ELSEVIER

Journal of Atmospheric and Solar-Terrestrial Physics ▮ (▮▮▮▮) ▮▮▮–▮▮▮

Journal of ATMOSPHERIC AND SOLAR-TERRESTRIAL PHYSICS

www.elsevier.com/locate/jastp

Initial results from the coupled magnetosphere–ionosphere–thermosphere model: thermosphere–ionosphere responses

W. Wang[a,*], M. Wiltberger[a], A.G. Burns[a], S.C. Solomon[a], T.L. Killeen[a], N. Maruyama[a], J.G. Lyon[b]

[a]*High Altitude Observatory, National Center for Atmospheric Research, Boulder, CO 80307, USA*
[b]*Department of Physics and Astronomy, Dartmouth College, Hanover, NH 03755, USA*

Received 29 January 2004; accepted 6 April 2004

Abstract

The thermosphere–ionosphere nested grid (TING) model has been successfully coupled with the Lyon–Fedder–Mobarry (LFM) global magnetosphere MHD code. The coupling between these models is two-way: the LFM provides the TING model with global electric fields and precipitating electron energy fluxes, and the TING model feeds ionospheric conductances back to the LFM. This code coupling enables studies of the global energy budget of the magnetosphere–ionosphere–thermosphere system. In this paper, we present simulation results from the coupled magnetosphere–ionosphere–thermosphere (CMIT) model under solar minimum, northern hemisphere summer conditions. The IMF input to the CMIT model changed its direction every 4 h. Comparisons are made between the simulated results of the CMIT model and those of the stand-alone TING model. It is found that the CMIT model predicted higher cross polar cap potential drops than the empirical model used by the stand-alone TING model. The energy input to the upper atmosphere by precipitating electrons, however, was much lower in the CMIT model during the southward IMF interval. The simulated responses of the thermosphere and ionosphere were also significantly different. As a result of the greater Joule heating calculated in the CMIT model, neutral temperatures and winds were significantly enhanced in the CMIT model in comparison with the stand-alone TING model.

Keywords: Magnetosphere; Ionosphere; Thermosphere; MHD; Modeling

1. Introduction

The Earth's thermosphere and ionosphere are a dynamically coupled system. This dynamical coupling involves not only physical and chemical processes of various temporal and spatial scales within the region, but also interactions with other parts of the atmosphere through mass, momentum and energy transfer. Lower atmosphere tides and gravity waves propagate upward through the middle atmosphere depositing energy and momentum in the lower thermosphere, affecting neutral winds, densities and temperatures in this region. The magnetosphere, which is largely controlled by solar wind properties, is also a significant energy and momentum source for the thermosphere–ionosphere (T–I) system,

*Corresponding author. Tel.: +1-303-497-2177.
E-mail address: wbwang@ucar.edu (W. Wang).

1364-6826/$ - see front matter © 2004 Elsevier Ltd. All rights reserved.
doi:10.1016/j.jastp.2004.04.008

especially during geomagnetic storms (e.g. Killeen, 1987). Electric fields mapped down along the magnetic field lines from the magnetosphere drive ion winds in convection cells in the high latitudes. These ion winds, in turn, push the neutrals in the same direction through ion-neutral collisions. Significant particle precipitation also occurs during storms, enhancing ionospheric plasma densities and introducing additional heating in the thermosphere.

The response of the thermosphere and ionosphere to these energy and momentum inputs from the magnetosphere is both global and dynamic. Joule heating, produced by collisions between ions and neutrals, is the major magnetospheric energy deposition process in the thermosphere and can greatly enhance neutral temperatures at high latitudes (e.g., Lu et al., 1995; Thayer et al., 1995). This heating causes upwelling of molecular rich air from lower altitudes and transports it to middle and lower latitudes in the post midnight sector, affecting global neutral wind circulation and neutral composition profiles (e.g., Prölss, 1980; Prölss, 1987; Burns et al., 1991; Fuller-Rowell et al., 1994). These changes in wind pattern and composition then modify the ion recombination rate causing ionospheric electron density variations. The variations in ion densities, in turn, affect ion-neutral coupling processes and thus the energy and momentum deposition rate in the upper atmosphere.

One of the most important factors controlling magnetosphere–ionosphere–thermosphere coupling is the ionospheric conductance. Field-aligned currents complete their circuit in the ionosphere, mostly through E- and lower F-region Pedersen currents. The ionosphere serves as a dynamic resistor or load for the whole current system. This load changes with variations of the background ionosphere and thermosphere caused, in part, by field-aligned currents. Precipitating particles, which carry these field-aligned currents, can significantly enhance E- and lower F-region electron densities and thus enhance ionospheric conductance, especially at night. This enhanced conductance in turn allows more current to flow into the ionosphere.

In addition to the energy and momentum coupling between the I–T system and the magnetosphere, mass flow between these regions also has significant role in coupling. During major storms, O^+ outflow is a significant mass source for the plasma sheet and inner magnetosphere (e.g. Hamilton et al., 1988; Daglis, 1997). The acceleration mechanism for ionospheric oxygen ions remains unclear. Nevertheless, the role of O^+ in the onset and recovery phases of storms and substorms were recently well established.

Therefore, it is important to view and investigate the magnetosphere–ionosphere–thermosphere as a complete system. However, in almost all previous space weather studies, the magnetosphere, ionosphere and thermosphere have been treated as separate systems. Empirical models are used to specify the necessary inputs from another region that limits the dynamic coupling between different regions. For instance, in global magnetospheric MHD simulations, ionospheric conductance is typically specified using the Robinson et al. (1987) model. In thermosphere and ionosphere simulations, on the other hand, magnetospheric electric fields and particle precipitation are defined using statistical models based on satellite or ground-based observations (e.g. Weimer, 1995; Richmond and Kamide, 1988).

There have been several studies linking magnetosphere MHD models with thermosphere/ionosphere models. Sojka et al. (1997) used MHD model outputs of the convection electric field and auroral electron precipitation to drive a time-dependent ionospheric model (TDIM) through a substorm. This coupling was, however, one way, since no ionospheric output was fed back to the MHD model. In addition, the TDIM used an empirical thermospheric model.

Another effort was that of Raeder et al. (2001). They coupled the UCLA global magnetosphere model with the coupled thermosphere–ionosphere model (CTIM) and applied the coupled models to a study of the January 1997 magnetic storm. The potential and precipitation determined by the magnetospheric code were the input to CTIM, and CTIM calculated conductances and neutral wind dynamo currents were then fed back to the magnetospheric code. A much more realistic electrodynamic and ionospheric response was simulated by the coupled model than when a simple parameterized ionospheric conductance model was used by the magnetospheric model.

Ridley et al. (2003) also linked a magnetosphere model with a thermosphere and ionosphere model. They fed thermospheric neutral wind generated currents back to the BATSRUS global magnetospheric model to study neutral wind flywheel effects (e.g. Lyons et al., 1985; Deng et al., 1991). They showed that the neutral winds caused about a 6% increase in the cross polar cap potentials under IMF B_z southward conditions and a small increase in the strength of the field-aligned currents. Under IMF B_z northward conditions, however, the ionospheric convection pattern was reduced on the duskside but enhanced on the dawnside by the thermospheric neutral winds. Peymirat et al. (1998, 2002) also examined neutral wind effects on the magnetosphere using a coupled inner magnetosphere–ionosphere–thermosphere electrodynamics general circulation model. They found that the neutral wind effects could change the magnetospheric plasma pressure by $\sim 20\%$, and shielding potential by $\sim 10\%$.

In this paper, we describe coupling the Lyon–Fedder–Mobarry (LFM) global magnetosphere MHD code with the thermosphere–ionosphere nested grid (TING)

model to create the CMIT model. We apply this model to a climatology study of the magnetosphere–ionosphere–thermosphere response to various solar wind conditions. A companion paper (Wiltberger et al., 2004) describes the magnetosphere simulation results and the coupling procedure in detail. In this paper we will focus on the response of the I–T system to the magnetospheric inputs. In Section 2, we briefly discuss each component of the CMIT model and how these models are coupled together. Descriptions and discussions of the simulations will be presented in Sections 3 and 4, and the results will be summarized in Section 5.

2. Models

The LFM global magnetosphere code solves time dependent, three-dimensional ideal MHD equations. Detailed descriptions of the model equations and numerical methods can be found in Fedder and Lyon (1987, 1995); Fedder et al. (1995); Lyon et al. (2004); and Wiltberger et al. (2004). The code has a non-uniform, distorted spherical grid that allows better resolution in regions like the magnetopause, the geomagnetic tail and the ionosphere. The grid, which has the same coordinate system as the solar magnetic (SM) system, covers a region that extends from 30 R_E upstream to 300 R_E tailward of the Earth in the X direction, which is perpendicular to the Earth's magnetic dipole axis. The radial distance in the lateral Y/Z directions is 100 R_E in each direction. The magnetic fluxes are evaluated on the surface of each cell, whereas electric fields are calculated on the edges of the cells. This guarantees that the divergence of the magnetic field is zero. The numerical boundary conditions of the LFM are: (1) solar wind data observed or specified for intended investigations at the upstream and lateral boundaries, (2) supersonic outflow at the back boundary, and (3) ionospheric specifications adapted from empirical models, or in this case the TING model for the near-Earth boundary.

The near-Earth boundary of the LFM code is set to 2.0 R_E for our coupling study. The location of the boundary is determined by two competing factors: the Alfven wave speed and the lower latitude boundary of the ionospheric footprint of the LFM. It is desirable to have the magnetospheric grid as close to the ionosphere as possible to cover a larger area of the thermosphere and ionosphere for M–I coupling. However, the Alfven wave speed also increases significantly as the magnetospheric grid approaches closer to the ionosphere. This decreases the maximum time step possible within the MHD code. The field aligned currents (FACs) calculated in the magnetospheric grid are mapped down along dipole field lines to the ionosphere from the LFM inner boundary. A series of empirical relationships, detailed in Wiltberger et al. (2004), are used to determine the Pedersen and Hall conductances needed to obtain the polar cap potential pattern. This potential is used as part of the inner boundary condition for the magnetospheric MHD code.

The TING model is an extension of the NCAR thermosphere–ionosphere general circulation model (TIGCM) (Dickinson et al., 1981; Roble et al., 1988). One or more levels of nested grids are included to simulate mesoscale and micro-scale processes occurring in the T–I system. A detailed description of the TING model can be found in Wang et al. (1999). In our current coupling study, however, the nested grid capability is not employed since we are focused primarily on global scale processes. The TING model solves self-consistently time dependent, three-dimensional, momentum, energy and continuity equations of major and minor neutral species of the upper atmosphere (O_2, N_2, O, NO, $N(^4S)$, $N(^2D)$) and O^+ transport equation. Chemical equilibrium is assumed to obtain densities of other ion species (NO^+, O_2^+, N_2^+, N^+) and electrons. Steady state energy equations are solved to obtain ion and electron temperatures. The TING model uses a spherical geographic coordinate system with a uniform latitude and longitude grid of 5° resolution. The vertical coordinate is pressure level with a half scale height increment. The model assumes hydrostatic equilibrium.

The inputs of the TING model are $F_{10.7}$ and its 81-day average as proxies for solar EUV and UV radiation, lower atmospheric tides, as well as electric fields and particle precipitation from the magnetosphere. Outputs from the TING model are global three-dimensional distributions of mixing ratios of major and minor neutral species, neutral velocities and temperatures, electron and ion densities and temperatures. Other important physical parameters, such as Joule heating and ionospheric conductivities, are also calculated self-consistently in the model.

In this paper, we use two implementations of the TING model, the stand-alone TING model and the CMIT model. The stand-alone TING model, in most cases, is run using empirical models that are driven by IMF data (Wang et al., 2001). The IMF data are converted into hemispheric power and cross polar cap potential, which are then used to specify the high latitude ion convection pattern (Heelis et al., 1982). The Reiff and Luhmann (1986) empirical relationship is used to convert IMF data to cross polar cap potential,

$$P = P_0 + a v_{sw} B_t \sin^3(\theta/2), \quad (1)$$

where $P_0 = 6.7$ and $a = 0.047$. v_{sw} is the solar wind speed in kilometers per second, and B_t is the magnitude of the IMF in nanoteslas. Both P and P_0 are in

kilovolts, and

$$\theta = \cos^{-1}(B_z/B_t).$$

Hemispheric power is based on the Foster et al. (1986) and Emery et al. (unpublished manuscript) statistical formula,

$$E = e^{(P/27.76)}, \quad (2)$$

where E is in GWs and P is the cross polar cap potential calculated by Eq. (1). The electron precipitation is also specified using these two parameters (Roble and Ridley, 1987).

In the CMIT model, coupling between the TING model and the LFM code was implemented at the top boundary of the TING model. This coupling procedure is explained in detail in Wiltberger et al. (2004); a brief description is provided here. The M–I coupling occurs in the magnetosphere–ionosphere coupler module. Field-aligned currents calculated by the LFM code are mapped down to ionospheric heights where the electric field (potential) is determined. The potential is then mapped back to the LFM code for magnetosphere calculations. Particle precipitation is specified using a formula that is based on the Knight relationship (Knight, 1983; Wiltberger et al., 2004). Field-aligned potential drops implied by the Knight relationship are not included in mapping the potential to the magnetosphere. Understanding the auroral acceleration region and its implication for the energy conservation issues raised by Thayer and Semeter (2004) is a significant problem for the development of coupled magnetosphere–ionosphere models, and a major focus of the CISM project (Lotko, 2004).

In implementing this procedure the cross polar cap potential and the characteristic energy and number flux of the precipitating electrons are written to a file by the magnetosphere–ionosphere coupler module (see Fig. 2 in Wiltberger et al., 2004). The magnetosphere–ionosphere coupler also transfers data from the LFM grid to the geographic coordinates that TING model uses, and vice versa. At each time step (2 min) the TING model reads these data from the file, and uses them to provide the potential and electron mean energy and number flux that are otherwise calculated by empirical formulae (Eqs. (1) and (2)). After the TING model advances one time step, it writes out the height integrated Pedersen and Hall conductances,

$$\Sigma_P = \int_z \sigma_P \, dz \quad \Sigma_H = \int_z \sigma_H \, dz, \quad (3)$$

which are then picked up by the waiting LFM code and put into the magnetosphere–ionosphere coupler module to calculate new cross polar cap potentials. The LFM code then advances until the next conductances are available.

The Pedersen and Hall conductivities are calculated in the TING model as follows:

$$\sigma_P = \sum_s \frac{q_e n_s}{B}\left(\frac{\nu_{en}\omega_e}{\nu_{en}^2+\omega_e^2} + \frac{\nu_{sn}\omega_s}{\nu_{sn}^2+\omega_s^2}\right) \quad (4)$$

$$\sigma_H = \sum_s \frac{q_e n_s}{B}\left(\frac{\omega_e^2}{\nu_{en}^2+\omega_e^2} - \frac{\omega_s^2}{\nu_{sn}^2+\omega_s^2}\right), \quad (5)$$

where $s = 1, 2, 3$, stands for O_2^+, O^+ and NO^+, respectively. These are the major species in the ionosphere. ω_e and ω_s are the gyrofrequencies for electrons and the sth ion, respectively. B is the strength of the Earth's magnetic field. ν_{en} is the electron neutral collision frequency, and ν_{sn} is the collision frequencies between the sth ion and the neutrals. q_e is the electron charge. The calculation of conductivities involves using the densities of major neutral and ion species, temperatures of ions, electrons and neutrals, and the strength of the magnetic field. All of these physical parameters are calculated self-consistently in the TING model.

3. Simulations

The IMF conditions that were applied to the CMIT model for this climatology study are shown in Fig. 1. IMF clock angles changed every 4 h. Bz changed from positive to zero to negative and back to zero, whereas By changed from zero to positive to zero to negative over the 16 h period. The IMF B_x component was assumed to be zero. The solar wind had a constant density of 5.0 cm^{-3} and a constant speed of 400 km/s towards the Earth. The day of year for the simulation was 140, corresponding to May 19/20. Solar minimum conditions were also assumed, with $F_{10.7}$ and the 81-day $F_{10.7}$ running mean being equal to 70.0. The solar wind data were applied only to the LFM code in the CMIT model. The TING model did not need IMF information to

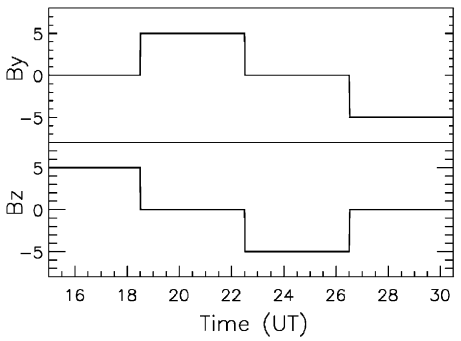

Fig. 1. Solar wind B_z and B_y components for the climatology study. The B_x component is set to zero throughout the simulation. The solar wind speed is 400 km/s and density is 5.0 cm^{-3}.

specify high latitude inputs since its magnetospheric inputs came directly from the LFM code as discussed in the previous section. The TING model was run for several model days to achieve a diurnally reproducible state by the time that coupling with the LFM began. In addition, appropriate monthly-averaged, semidiurnal tides were also applied to the lower boundary of the TING model to account for the impact of the lower atmosphere on the T–I system.

Fig. 2 gives the cross polar cap potential drop (Fig. 2a) and the energy flux (Fig. 2b) obtained from the M–I coupler module of the CMIT model. These data were applied to the TING model. It is evident that the potentials showed significant temporal variations throughout this simulation, whereas the energy fluxes were much smoother for almost the entire period, except during the B_z negative interval. In Fig. 2a the dashed lines are for the northern hemisphere and the solid lines are for the southern hemisphere, respectively. Heavy lines show total potential drops, whereas thin lines are maximum positive and minimum negative values. Potentials varied almost immediately after IMF changed its direction. The total potential drops in the southern hemisphere were slightly higher than those of the northern hemisphere when B_z was zero and B_y was 5. The differences of potentials between the two hemispheres were much larger later in the simulation (for the $B_y = -5$ and $B_z = 0$ case). During most of the time when B_z was negative the total potential drops were roughly the same for the southern and northern hemispheres. The interhemisphere variability exhibited here in the coupled model requires further investigation. It is generally believed that summer hemisphere (Northern hemisphere in this simulation) should have less cross polar cap potential drop, since the higher daytime conductance reduces the potential for the same magnitude of the currents flowing into each hemisphere. The magnitude of the positive cell of the convection pattern exceeds that of the negative cell during the B_z negative period (Fig. 2a). This is opposite to the prediction of the Weimer model for similar IMF conditions (Weimer, 1995). This discrepancy clearly needs to be addressed in future studies.

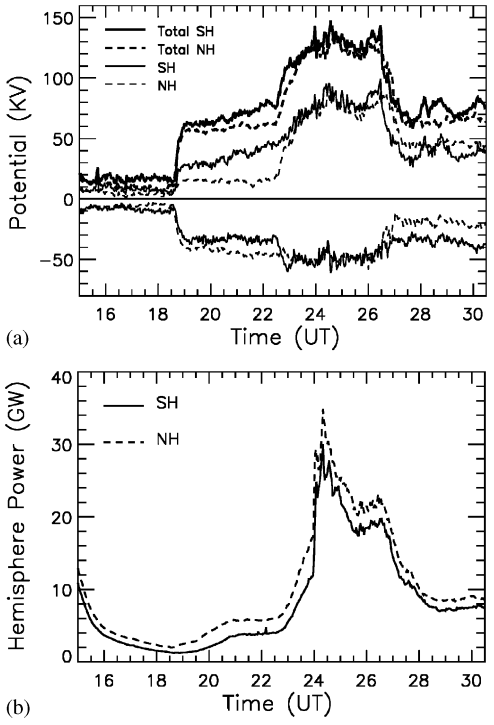

Fig. 2. Cross polar cap potential (panel a) and hemispheric power (panel b) inputs to the TING Model from LFM code for southern (SH) and northern (NH) hemispheres.

The total precipitating particle energy inputs to each hemisphere are shown in Fig. 2b. The dashed line gives values for the northern hemisphere and the solid line gives values for the southern hemisphere, respectively. The total hemispheric power input to each hemisphere was roughly the same, but the southern hemisphere received slightly more energy throughout the entire simulation. It is interesting to note that the changes in hemispheric power lagged behind the IMF direction changes by about one and a half hours after B_z turned southward. This corresponds to the time that is needed for the magnetosphere to store enough energy from the solar wind to produce a substorm onset. The growth phase is seen to occur at 22:30 UT immediately after IMF B_z turned southward and lasted till $\sim$ 24:00 UT when a substorm onset occurred, which was followed by subsequent expansion and recovery phases. Therefore, the coupled model is able to provide the timing of the growth, onset and recovery phases of substorms to the TING model, which is crucial for space weather forecasting. This information is not available from most of the empirical inputs used in the current thermosphere–ionosphere models (see Fig. 3). It is also interesting to note that the cross polar cap potential remained at roughly the same level for the entire IMF B_z southward period, despite exhibiting numerous small variations, but dropped immediately after B_z became zero. The hemispheric power, however, showed significant changes in magnitude when B_z was negative, and in addition, took more time to attain steady values again after 02:30 UT when B_z was no longer negative.

Fig. 3 shows high latitude inputs for the stand-alone TING model run (solid lines). Cross polar cap potential is in the upper panel and hemispheric power is in the lower panel, respectively. For comparison, potential and hemispheric power (averaged over two hemispheres) from the CMIT model are also plotted in Fig. 3 (dashed lines). Eqs. (1) and (2) were used to derive the potential and the hemispheric power from the solar wind data

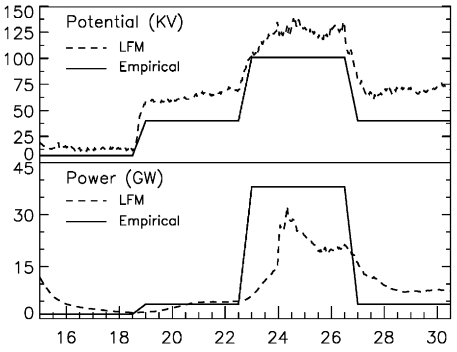

Fig. 3. Cross polar cap potential (upper half) and hemispheric power (lower half) inputs to the stand-alone TING Model (solid lines). The CMIT model outputs averaged over two hemispheres (Fig. 2) are plots for comparison (dashed lines).

shown in Fig. 1. A 30-minute time delay was added to the potential and the hemispheric power when IMF turned from one direction to another. This delay was roughly the same as the time that it took for the polar cap potential to response to IMF changes in the CMIT model (see Fig. 2a). It is evident that the potentials from the CMIT model were higher than those calculated by the empirical model. The potentials during By $= \pm 5$ periods were about 65 kV for the CMIT model, but 38 kV for the empirical inputs. During the B_z negative period (22:30 UT to 02:30 UT) the CMIT model potential was roughly constant around 125 kV with small variations, whereas the potential calculated by the empirical formula stayed flat at 100 kV. These differences in potentials have significant implications for thermosphere–ionosphere simulations since they affect the efficiency of ion-neutral coupling and energy and momentum transfer from the magnetosphere to the T–I system

Hemispheric power, which is used as a proxy for high latitude particle precipitation, behaved quite differently from the potential. The CMIT model had roughly the same hemispheric power as the stand-alone TING model throughout most of the simulation, except when intense energy input to the T–I system occurred during the B_z southward period. A substorm onset was evident after about 24:00 UT in the CMIT model, but when empirical models were used to define the inputs this behavior could not be replicated. The empirical models just increased the energy input immediately after the southward turning of the IMF. It is also evident that, on average, the hemispheric power was significantly lower in the CMIT model than it was in the stand-alone TING model. The power input from the empirical model into the stand-alone TING model was about two times larger than the power that was transferred from the LFM code to the TING component of the CMIT model.

Ion convection patterns at 22:00 UT are shown in Fig. 4. In the CMIT model, the cross polar cap potential was about 80 kV in the southern hemisphere and 60 kV in the northern hemisphere (Fig. 2a). These variations in the polar cap potential resulted from different conductances in the two hemispheres. The northern hemisphere was predominantly sunlit and thus had higher conductances than the southern hemisphere which was mainly in darkness. Fig. 4a and b illustrate the northern and southern hemisphere ion drifts that were calculated by the CMIT model. A dominant dusk convection cell in the northern hemisphere and a strong dawn convection cell in the southern hemisphere were seen, in agreement with observations and empirical models under B_y positive and B_z zero conditions (e.g., Weimer, 1995). This is different from the B_z negative case we discussed earlier where a significant discrepancy was found. There were a few instances of noticeable ion drift velocities near the low latitude boundary of the potential solver (45° magnetic latitude) at 01:00 LT (local time) (Fig. 4a) that were not physically real. They were caused by a boundary effect in solving the potential that resulted from assuming zero potential at the lower latitude boundary. A global potential solver in being developed to deal with this problem. The ion convection patterns for the stand-alone TING model are shown in Fig. 4c and d for the northern and southern hemispheres, respectively. These patterns showed structures that were quite similar to those seen in the CMIT model. IMF B_y effects on the convection pattern were also evident. The empirical convection pattern had significantly smaller ion drift velocities, because the cross polar cap potential was almost 20 kV smaller in the empirical model. Nevertheless, it is important to note that CMIT model outputs (potentials and energy fluxes) were in the same range as those of the empirical models, and that the structures and variations with geophysical conditions were also similar to those predicted by the empirical models. This indicates that our coupling scheme is working and producing reasonable results. On the other hand, the CMIT model captured the dynamical response of the magnetosphere, thermosphere and ionosphere system to IMF inputs even though the inputs to the system were steady.

At 02:00 UT (26:00 h model time) both the CMIT model and the stand-alone TING model had much stronger ion convection patterns than those at 22:00 UT (Fig. 5a and b). A substorm occurred after B_z turned southward at 22:30 UT. Cross polar cap potentials were 125 kV for the CMIT model and 100 kV for the stand-alone TING model. The convection pattern in the CMIT model was stronger and broader than that in the stand-alone TING model. This is an expected result since higher cross polar cap potentials were predicted in the CMIT model.

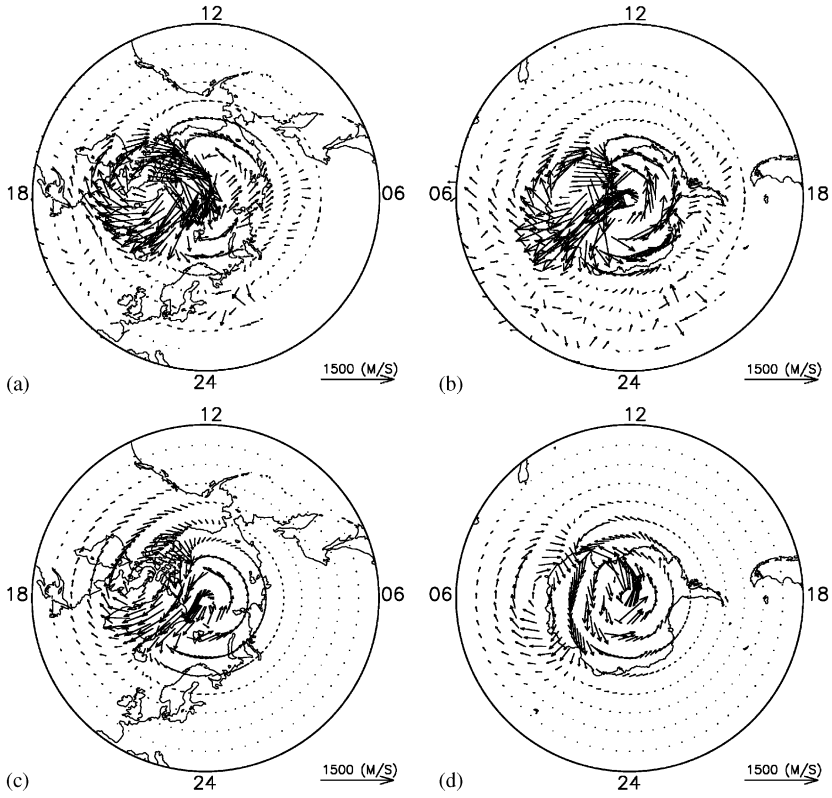

Fig. 4. Ion convection patterns at 22:00 UT for northern (left panels) and southern (right panels) hemispheres. The upper panels shows the CMIT model results and the lower panels show the stand-alone TING Model results with empirical model forcing.

There was almost a factor of two difference in hemispheric power between the two models, as shown in Fig. 2b. This implies that the stand-alone TING model received more precipitating energy than the CMIT model (Fig. 5c and d, for the northern hemisphere). Precipitation covered a wide region of the high latitudes at night, but no precipitation occurred during the daytime (Fig. 5c) in the CMIT model. Two regions of strong precipitation were seen just around the local midnight. The highest energy flux was close to $1.8\,\mathrm{erg\,cm^{-2}\,s^{-1}}$. On the other hand, the precipitation pattern specified for the stand-alone TING model had a higher energy flux, with the maximum being greater than $3.0\,\mathrm{erg\,cm^{-2}\,s^{-1}}$. The strongest precipitation occurred in the pre-midnight sector, which is consistent with the behavior of the CMIT model. A detailed description of the techniques used to specify the auroral oval from the hemispheric power and cross polar cap potential can be found in Roble and Ridley (1987). It is also notable that the "islands" seen in Fig. 5d are not the results of the model specification, rather they are the numerical manifestation of the grid discretization effect (Wang et al., 1999) due to the low spatial resolution of the model. The differences in the ion convection patterns significantly impact the structure of the thermosphere and ionosphere, as will be discussed in detail in the next section.

Height integrated Pedersen (left panel) and Hall (right panel) conductances in the northern hemisphere at 02:00 UT (26:00 h model time) are illustrated in Fig. 6 for both the CMIT model and the stand-alone TING model. It is obvious that both Pedersen and Hall conductances are produced by two mechanisms: daytime solar EUV radiation and nighttime particle precipitation. Solar EUV photons ionize neutral particles in the thermosphere and produce ions and electrons above 90 km. Contributions to the conductances mostly come from the E- and lower F-region, where electrons are controlled by the magnetic field, but ions flow with the neutrals. The E-region is approximately in photochemical equilibrium and disappears at night due to rapid recombination after sunset. However, at high latitudes, precipitating energetic electrons and ions with characteristic energy in the range of a few hundred eV to tens of keV can penetrate deep into the upper atmosphere and produce a significant amount of ionized gas at E-region heights. Therefore, daytime conductances show strong solar zenith angle variations as well as neutral

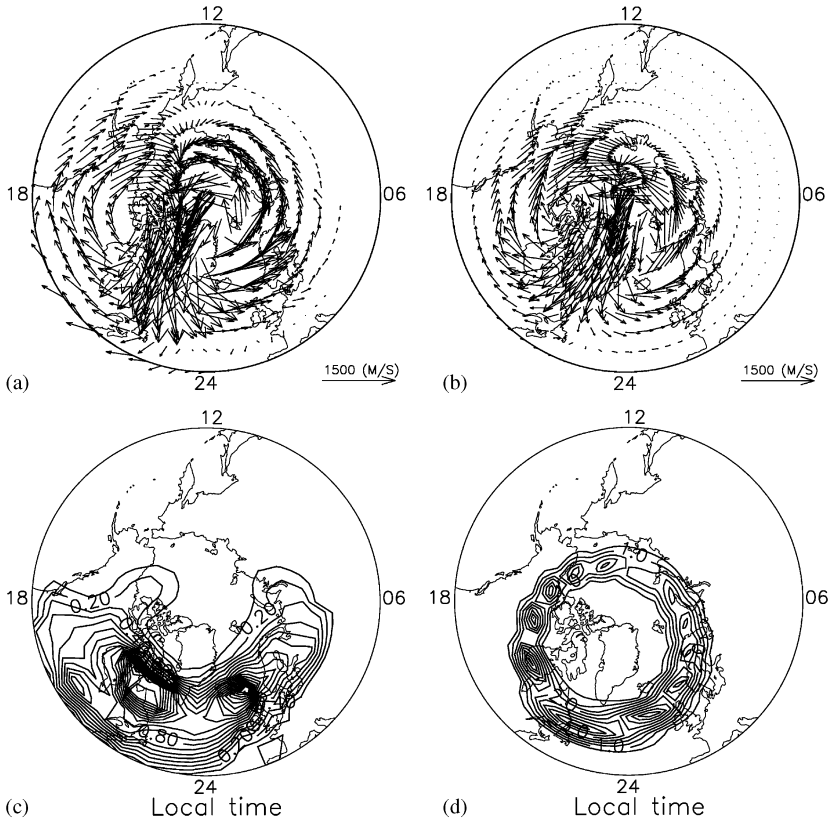

Fig. 5. Ion convection patterns (upper panels) and precipitating particle energy flux (erg cm^{-2} s^{-1}, lower panels) at 02:00 UT. The results from the CMIT model are illustrated on the left, and those from the stand-alone TING model on the right.

thermospheric effects, whereas nighttime conductances are mainly determined by the number of precipitating particles and their characteristic energy.

In the stand-alone LFM code, ionospheric conductances are specified using a very simple empirical model. The dynamical response of the T–I system is not included in this conductance model. The CMIT model allows us to self-consistently investigate the dynamic link among various regions, especially the feedback effect of the ionospheric conductance variations on global magnetospheric structures (Wiltberger et al., 2004). In Fig. 6 Pedersen and Hall conductances from the CMIT model and stand-alone TING model were almost exactly the same in the daytime middle latitudes, indicating that high latitude energy and momentum inputs from the magnetosphere were not intense enough to penetrate to lower latitudes and affect the ionospheric electron density profiles there. Hall conductance was higher than Pedersen conductance. At high latitudes, the stand-alone TING model produced more conductances than the CMIT model since higher energy fluxes were input in the stand-alone TING model (cf. Fig. 3). The maximum Hall conductance in the CMIT model was 12.7 mhos, whereas that in the stand-alone TING model was 21.6 mhos, almost a factor of two difference, similar to the ratio seen in hemispheric power in the two versions of the model (see Fig. 3). The conductance patterns were also similar to those of the particle precipitation shown in Fig. 5.

4. Thermosphere response

The thermosphere sustains a global wind circulation that is driven mainly by five forces: pressure gradient, ion drag, the Coriolis force, advection and viscosity. The contribution from each force to the overall force balance varies with geophysical conditions as well as geographical locations and altitudes (e.g., Killeen and Roble, 1984). At ionospheric F-region heights the pressure gradient force and ion drag are the dominant forces that drive the high latitude neutral winds. Ion drag pushes the neutrals in a convection pattern that is similar to that of the ions. The neutral wind circulation then moves air parcels of different densities and species around, modifying global thermospheric neutral density

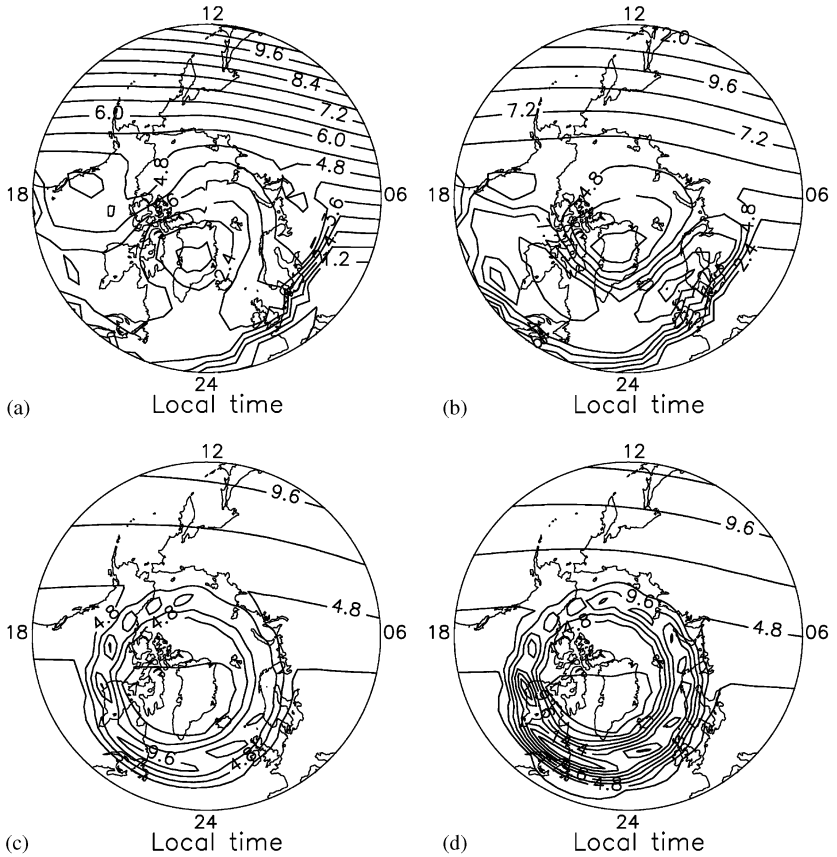

Fig. 6. Height integrated Pedersen (left panels) and Hall (right panels) conductances (mho) at 02:00 UT. Results from the CMIT model are shown in the top panels, and those from the stand-alone TING model are shown in the lower panels. The contour interval for the CMIT is 0.6 mho, while that for the stand-along-TING model is 2.4 mho.

distributions and ionospheric profiles (e.g. Burns et al., 2004; and references therein).

Joule heating increases the neutral temperature, and thus enhances pressure gradients and neutral winds. This heating causes molecular rich air to upwell from lower altitudes, which changes plasma densities through enhanced ion recombination processes. Joule heating is calculated as follows,

$$Q_J = \sigma_P(\vec{E} + \vec{u}_n x \vec{B})^2, \quad (6)$$

where $\vec{E}$ is the imposed magnetospheric electric field, $\vec{B}$ is the geomagnetic field and $\vec{u}_n$ is the neutral wind velocity. Therefore, three factors determine the magnitude of Joule heating: the strength of the electric field (or ion drift velocity), the neutral wind velocity and the Pedersen conductivity. Now, if we assume that at high latitudes magnetic field is only in the vertical direction, Eq. (6) can then be rewritten as,

$$Q_J = \sigma_P B^2((U_i - U_n)^2 + (V_i - V_n)^2), \quad (7)$$

where U_i, V_i, are ion zonal and meridional drift velocities, and U_n, V_n are neutral zonal and meridional wind velocities, respectively.

Figs. 7 and 8 illustrate neutral winds on top of neutral temperature contours at pressure level -0.5 (~ 200 km) for four UT times. Fig. 7 gives these values for the CMIT model and Fig. 8 gives them for the stand-alone TING model. Figs. 7a and 8a show neutral winds and temperatures at 18:00 UT. At this time B_y was zero and B_z was positive. The imposed magnetospheric electric fields were weak, the cross polar cap potentials were around 10 kV in both the CMIT model and the stand-alone TING model, and the hemispheric power was small. Both plots thus show very similar structures. The thermosphere and ionosphere were controlled primarily by solar radiation at this time because the magnetospheric inputs were weak. These high daytime neutral temperatures drove day to night pressure gradient winds. Highest temperatures occurred in the afternoon. There was also a very weak neutral convection cell in the

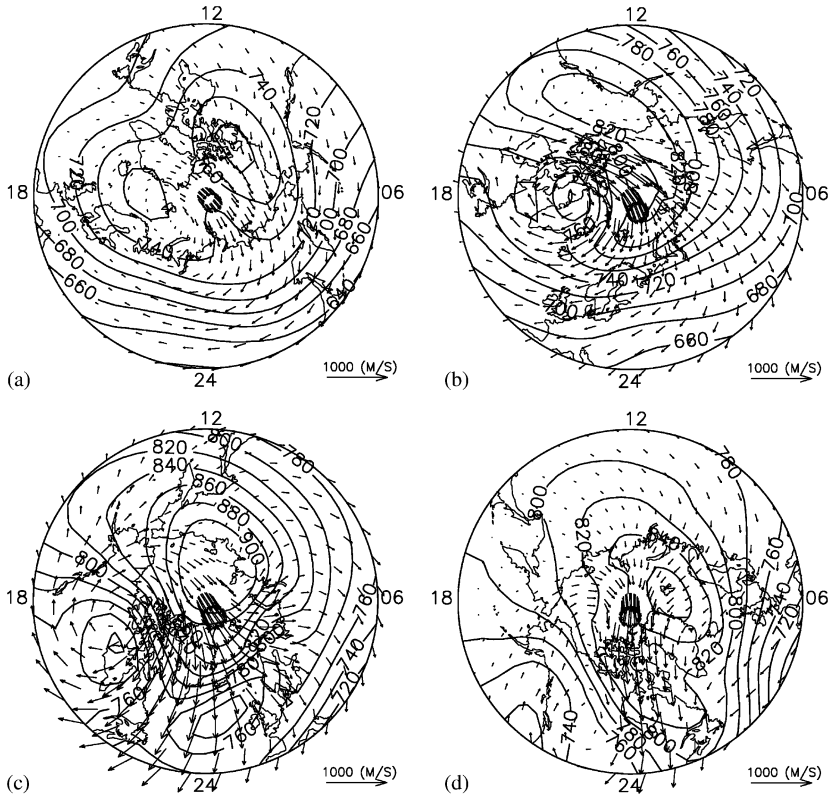

Fig. 7. Neutral temperatures and winds at pressure level −0.5 (~ 200 km) simulated by the CMIT model for 18:00 UT (panel a), 22:00 UT (panel b), 02:00 UT (panel c) and 06:00 UT (panel d), respectively.

dusk side in both the coupled and the stand-alone models, which was probably a residual of the convection pattern before B_z turned northward.

Four hours later at 22:00 UT, the neutral winds and temperatures simulated by the CMIT model and the stand-alone TING model began to diverge. As shown in Fig. 3 significant cross polar cap potential was imposed on the CMIT model, but not on the stand-alone TING model. Hemispheric power inputs were roughly the same for both models. The neutral temperatures and winds from the stand-alone TING model did not show significant changes compared with those at 18:00 UT (Figs. 8a and 8b). The speeds of the neutral winds were almost the same, except in the dusk convection cell; neutral temperature increases in the afternoon sector at middle latitudes ranged between 20 and 40 K. These probably resulted from a UT effect induced by the movement of the geomagnetic pole and its associated high latitude convection pattern around the geographic pole. Significant Joule heating occurred in the afternoon sector at this UT and earlier times (Fig. 10a). This heating was caused by a strong ion drift pattern sweeping through regions of high daytime Pedersen conductivities. In addition, very few temperature changes occurred at night.

Significant changes, however, were seen in the CMIT model calculations for this UT hour (Fig. 7b). The neutral wind dusk convection cell was evident and wind speeds were significantly higher than that at 18:00 UT. Neutral temperature enhancements occurred globally. In the daytime polar cap region neutral temperature increases of 60 K occurred. In other places neutral temperatures increased by about 40 K in both daytime and nighttime.

Similar results were also obtained at 02:00 UT (26:00 h model time). These results are shown in Figs. 7c and 8c. Prior to this time the magnetosphere had experienced multiple onsets of geomagnetic substorms, thus significant amounts of energy had been deposited in the thermosphere and ionosphere both through particle precipitation and the strong electric field that was generated. In the stand-alone TING model the neutral temperature was seen to have a global 20 K increase compared with that at 22:00 UT, and the neutral wind speeds were also significantly higher. However, these changes were not as big as those that occurred in the

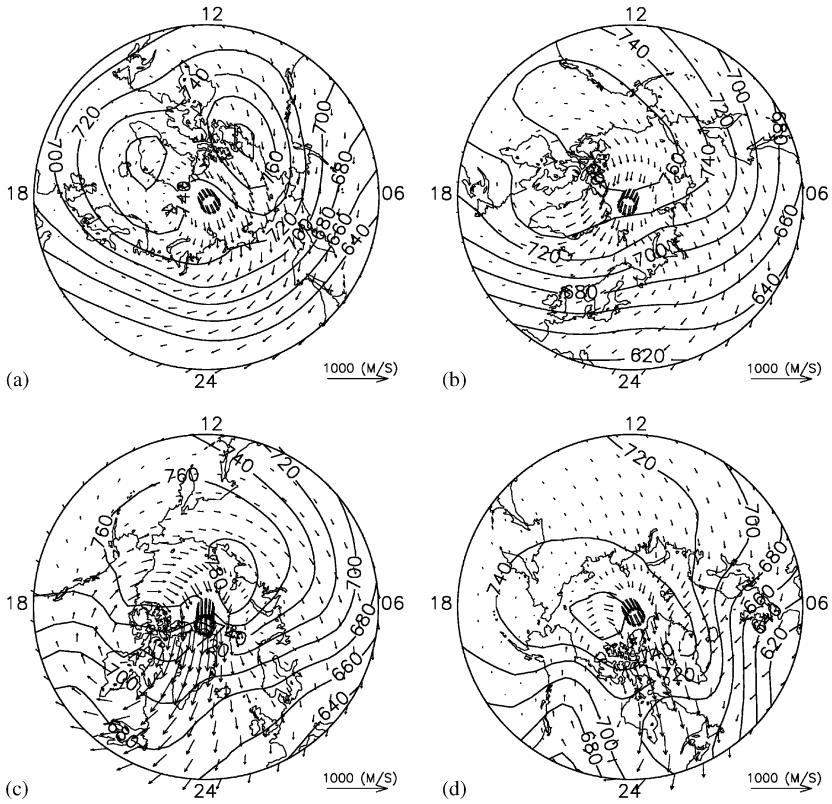

Fig. 8. Same as Fig. 7, but for the stand-alone TING model.

CMIT model. A maximum temperature of 920 K occurred in the coupled model that was 100 K higher than the temperature at 22:00 UT and 160 K hotter than that at 18:00 UT. This was significantly higher than the temperature simulated by the stand-alone TING model. Another interesting phenomenon calculated in the CMIT model was that two regions of low temperatures occurred in the nighttime, one located at about 20:00 LT and another one at 01:00 LT. These probably resulted from cooling by expansion. Neutral winds were intensified globally in both the coupled and the stand-alone models and had very similar patterns, though the speed of the wind simulated by the CMIT model was significantly higher than that calculated by the stand-alone TING model, in part because the simulated cross polar cap potential was much stronger in the CMIT model (Fig. 3).

At 06:00 UT (30:00 h model time), B_z was zero and B_y was negative, and both the potential and hemisphere power inputs to the thermosphere and ionosphere were reduced from the B_z negative conditions that prevailed at 02:00 UT. Neutral temperatures in the CMIT model (Fig. 7d) decreased by about 60 K from their previous values at 02:00 UT, but were still significantly higher than those at 18:00 UT, indicating that significant Joule heating was still occurring. The stand-alone TING model, on the other hand, predicted that neutral temperatures had almost returned to their initial values at 18:00 UT, albeit with some local time variations (Fig. 8d). Strong anti-sunward flow was still the dominant feature in the neutral wind circulation. However, the return flow of the neutral wind dusk convection cell was significantly weakened as a result of the B_y negative conditions that produced a weak dusk ion convection cell.

To fully understand the simulated neutral temperature differences between the CMIT model and the stand-alone TING model, the Joule heating rates per unit mass (K/day) at the same pressure level ($\sim$ 200 km) calculated by each model are illustrated in Figs. 9 and 10, respectively. For the purpose of this study it is desirable to use Joule heating rate per unit mass rather than Joule heating per unit volume to describe the effects of Joule heating on the neutral atmosphere because this form of the Joule heating rate is more closely related to the modeled temperature changes. Fig. 9a–c show the Joule heating rate from the CMIT model for UT 22:00, 02:00 and 06:00, respectively, whereas Fig. 10a–c are those from the stand-alone TING model for the same times. The contour interval is 600 K/day in both plots. The

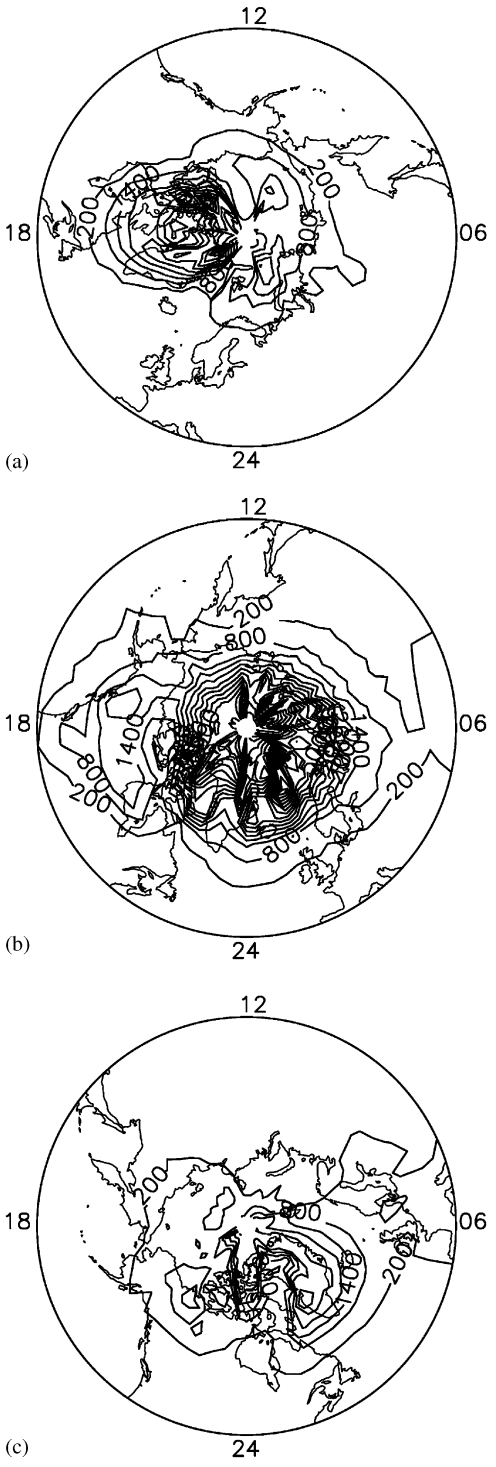

Fig. 9. Joule heating rate (K/day) at pressure level −0.5 (~ 200 km) simulated by the CMIT model for 22:00 UT (panel a), 02:00 UT (panel b) and 06:00 UT (panel c), respectively. The contour interval is 600 K/day.

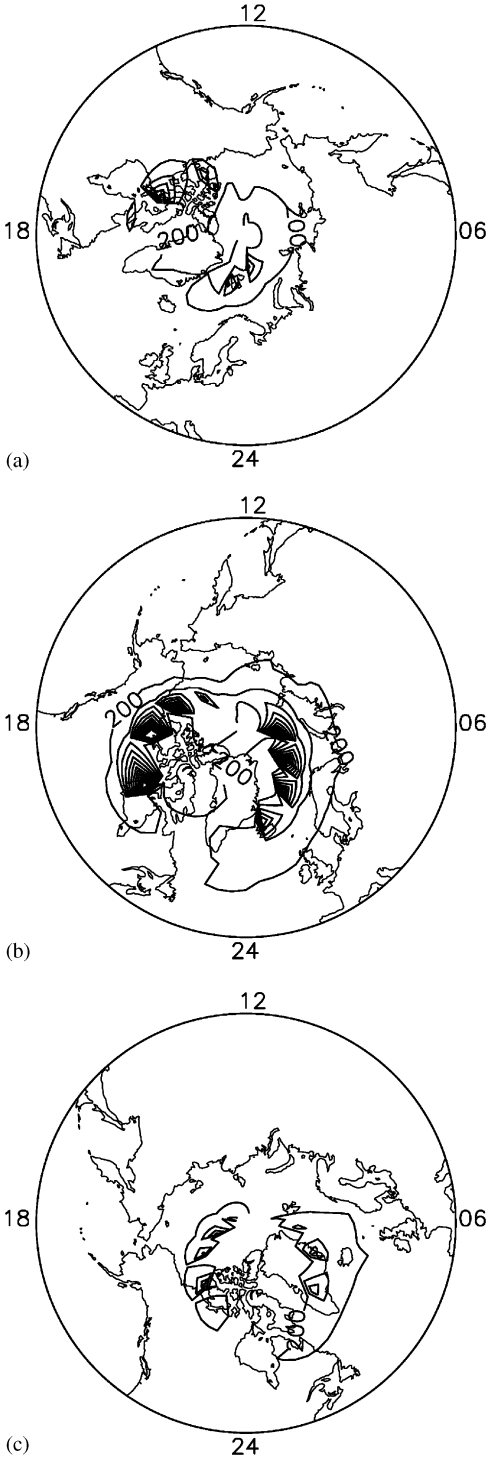

Fig. 10. Same as Fig. 9, but for the stand-alone TING model. The contour interval is 600 K/day.

Joule heating calculated by the CMIT model occurred over a much broader area than that calculated by the stand-alone TING model at all times due to the broader ion convection and electron precipitation patterns imposed in the CMIT model (cf. Figs. 4 and 5). On the other hand, Joule heating in the stand-alone TING model is confined to a very limited area around the polar cap. Furthermore, the magnitude of Joule heating in the CMIT model was, in general, much higher than that of the stand-alone TING model. It is worthwhile noting that the plots shown here give only the instantaneous pictures of Joule heating at this particular time. The neutral temperatures shown in the previous plots (Figs. 7 and 8) are the result of the integrated effect of various heating and cooling processes. Joule heating contributes significantly to the changes in neutral

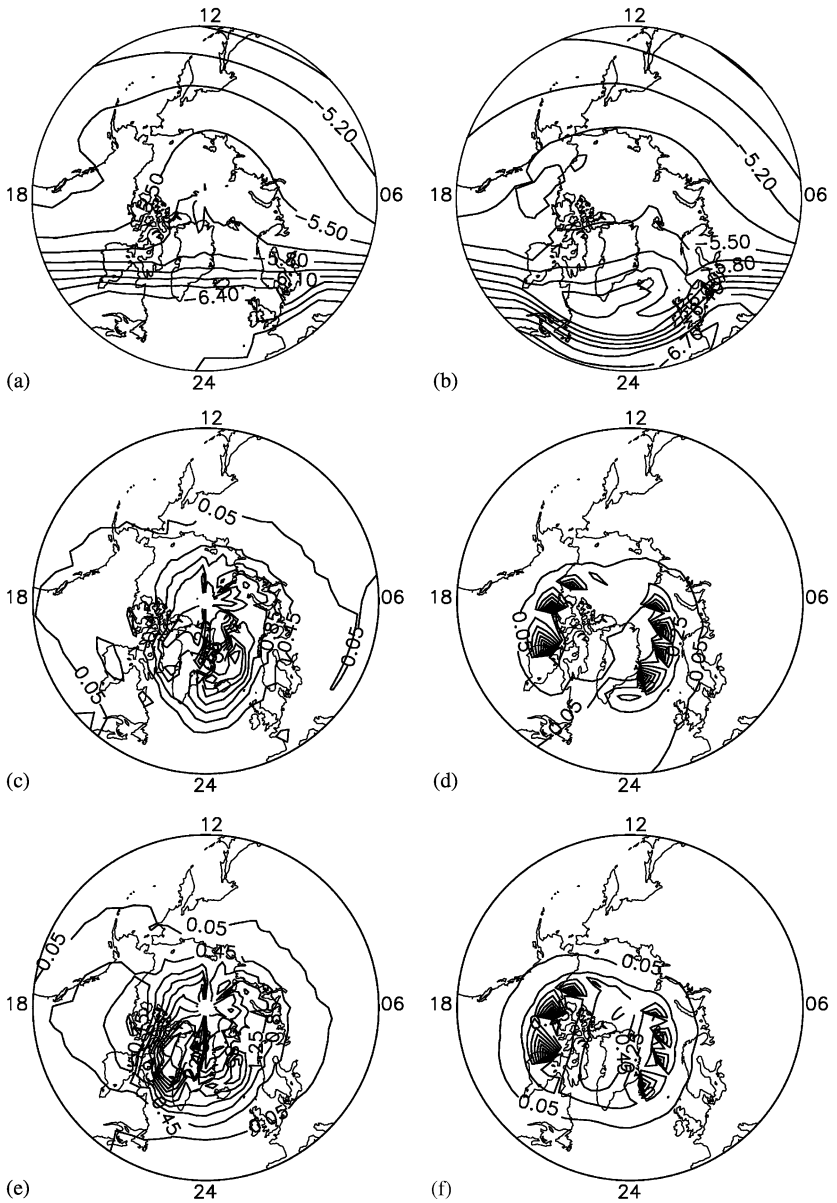

Fig. 11. Ionospheric conductivity (mho/m, upper panels) at 02:00 UT on pressure level −0.5 (~ 200 km). The middle panels show $(U_i - U_n)^2 + (V_i - V_n)^2$ (km/s)^2, and lower panels are $U_i^2 + V_i^2$ (km/s)^2, where U_i, V_i, are ion zonal and meridional drift velocities, and U_n, V_n are neutral zonal and meridional wind velocities, respectively. Left panels are the results from the CMIT model, while right panels are those from the stand-alone TING model.

temperatures. However, the global structure of the neutral temperature is determined by the balance between a variety of heating and cooling processes.

Several factors contribute to these differences in Joule heating (Eqs. (7) and (8)). The left panels of Fig. 11 illustrate the Pedersen conductivity (upper panel), the square of ion-neutral relative velocities (middle panel, in units of $(km/s)^2$), and the square of ion velocities (lower panel, in units of $(km/s)^2$), respectively, at pressure level −0.5 and 02:00 UT for the CMIT model. The same physical parameters calculated by the stand-alone TING model are plotted in the right panels. It is evident from Fig. 11a and b, that at high altitudes, the differences in the conductivities between the two models are smaller than the differences at lower heights. This is understandable since electron density enhancements produced by the precipitating particles are most pronounced at E region heights. Comparing Figs. 9b and 10b with Fig. 11c and d, it is easily seen that the square of the relative velocity between the ions and neutrals is the most significant contribution to the differences in the Joule heating rate between the two models. The Joule heating pattern follows that of the square of the relative velocities. The ion drifts calculated by the CMIT model are significantly higher than those from the stand-along TING model (Fig. 5). The potential in the CMIT model has larger gradients than the empirical model used in the stand-alone TING model. This, in turn, generates stronger ion drifts in the CMIT model. Fig. 11e and f are the plots of the square of the ion velocities for the CMIT model and the stand-alone TING model, respectively. Those two plots illustrate neutral wind effects on Joule heating when compared to Fig. 11c and d. Joule heating is decreased in both models when neutral winds are included in the Joule heating rate calculations (cf. Eq. (8)). The most significant changes occurred inside the polar cap in the antisunward flow region, where both ions and neutrals moved in the same direction from the dayside to the nightside (see Fig. 5a and b for the ion drifts, and Figs. 7c and 8c for the neutral velocities). Fig. 11e illustrates that there was significant Joule heating in the CMIT model between 21:00 and 22:00 LT if neutral winds were not included, but this heating almost disappeared when neutral winds were included. The same observation can also be applied to the stand-alone TING model, in which Joule heating was almost absent in the antisunward flow region if neutral winds were included (Fig. 11d and f).

The neutral wind effect was also evident in the total hemispheric Joule heating plot (Fig. 12). Joule heating increased immediately after B_z turned southward at 22:30 UT. It is difficult to estimate the neutral wind effect in the CMIT model since ion drift velocities varied significantly even when the IMF input was kept steady (Fig. 2a). However, the potential in the stand-alone TING model was the same after 22:30 UT and so were the ion drift velocities and particle precipitation. The solid line shown in Fig. 12 represents the total Joule heating in the stand-alone TING model. It shows clearly that, after the initial burst of the Joule heating at 22:30 UT, Joule heating decreased with time from the peak value of about 160 GW at about 23:00 UT to its minimum value of about 120 GW at 02:30 UT when IMF B_z became zero. This indicates a drop of about 25% in the total Joule heating input during the steady IMF B_z southward conditions. Most of these changes in total Joule heating can probably be attributed to variations in the neutral winds. It usually takes a couple of hours for the neutrals to fully respond to changes in ion motion (Ponthieu et al., 1988). Thus, if the ion convection pattern was in a steady state for several hours, neutral winds were becoming more like the ion winds as a result of ion drag, and, therefore, the relative velocity between the ions and neutrals was becoming lower with time, resulting in a gradually decreasing Joule heating rate. This is evident in the stand-alone TING model simulations shown in Fig. 12. One the other hand, the ion convection pattern varied with time in the CMIT model, and the neutral winds effect on the total Joule heating was thus very difficult to evaluate (Figs. 2 and 3). However, Fig. 11e and 11c do indicate that neutral winds decreased the Joule heating input to the upper atmosphere. The effects of ion convection variability on Joule heating were also discussed recently by Matsuo et al. (2003) and Codrescu et al. (2000). It is, however, worthwhile to mention here that conductivities also changed with time as the thermosphere responded to energy input from the magnetosphere, and also that the background thermosphere and ionosphere near the auroral oval changed with UT. This may also contribute to variations in the total Joule heating (Fig. 12). The total Joule heating simulated in the CMIT model was about 3–4 times higher that in the stand-alone TING model, which, in turn, contributed to the higher neutral

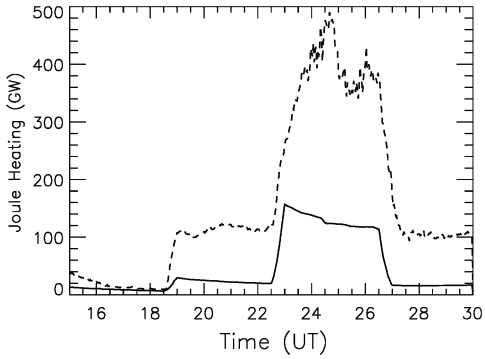

Fig. 12. Hemispheric joule heating (GW) calculated by the CMIT model (dashed line) and the stand-alone TING model (solid line).

temperature calculated in the CMIT model (Fig. 7). The differences, as mentioned before, were in the ion drift velocities or electric fields calculated by each model. The CMIT model simulated higher cross polar cap potential, and most importantly, larger spatial gradients in the potential pattern that produced stronger electric fields. It is very important to have the right high latitude energy inputs to the upper atmosphere since, as discussed in the introduction, the thermosphere and the ionosphere response both actively and globally to this energy input. To validate the global structures and temporal variations of the thermosphere and ionosphere predicted here by both models is one of the major tasks of the CISM project (Spence et al., 2004).

5. Summary

The LFM global magnetosphere code has been successfully coupled with the TING model. The coupling between these models is two way: the LFM provides the TING model with high latitude cross polar cap potential and precipitating electron energy flux, and the TING model feeds back height integrated conductances. The physical parameters calculated by the CMIT model, i.e., conductances, potentials and energy fluxes, agree in general with those obtained from statistical empirical models. The following conclusions are drawn from this climatology study:

1. Energy input from the magnetosphere has a significant impact on thermosphere–ionosphere structures both locally and globally. The study here and that in the companion paper (Wiltberger et al., 2004) demonstrates the capability of the coupled magnetospheric model and thermosphere/ionosphere model to investigate the global energy budget in the entire magnetosphere–ionosphere–thermosphere system. Unlike empirical models of the high latitude potential and energy flux, which either tend to smooth out or are unable to simulate spatial and temporal variations of these parameters, the CMIT model can simulate their dynamic variability.
2. The coupled model is able to provide the thermosphere–ionosphere model with the timing of the growth, onset and recovery phases of substorms. Empirical models have significant difficulties in predicting this timing.
3. During B_z positive conditions the high latitude ionosphere and thermosphere were almost undisturbed by the weak magnetosphere input. They showed features that were dominated by solar radiation in both the CMIT model and the stand-alone TING model simulations.
4. During B_z negative conditions a significant amount of energy was deposited in the upper atmosphere. Ion drifts were greatly enhanced at high latitudes. Neutral temperatures were increased by almost 160 K more in the coupled model than in the B_z positive case.
5. The stand-alone TING model did not predict the large neutral temperature and wind enhancements seen in the CMIT model simulations during substorms. This can be explained by the different Joule heating rates in the two versions of the model. Joule heating calculated by the CMIT model was much stronger than that in the stand-alone TING model because of the high cross polar cap potential and, most importantly, its larger spatial variations simulated by the coupled model.
6. The electron precipitation energy input from the LFM code to the TING model is lower than that from the statistical model by a factor of two. When the LFM model is used, the conductances calculated by the TING model are much lower than the conductances calculated when statistical inputs are used.

The CMIT model is able to capture the instantaneous state of the global high latitude electric field, whereas the stand-alone TING model is capable only of simulating averaged electric field patterns. This has very significant implications for our future studies of the global energy budget in the whole magnetosphere, ionosphere and thermosphere system. Firstly, current space and ground based measurements of electric fields, both directly or indirectly, frequently mix up spatial and temporal variations and lack global coverage of the electric field. The CMIT model can supply the thermosphere/ionosphere model with not only the global electric field itself, but also its temporal and spatial variations, allowing a realistic estimation of energy deposition in the upper atmosphere to be made. Secondly, the feedback of ionospheric conductances calculated by first principles models has the potential to permit a better estimation of the electric field than that obtained from the empirical ionospheric conductance models that are currently used in magnetospheric MHD codes. This makes the study of the dynamical impact of the ionosphere on the magnetospheric currents system and global magnetospheric structures possible. Finally, the CMIT model allows a better estimation of the timing of the substorm onset than is obtainable from empirical models for space weather applications. The exact timing of the commencement of substorms has a significant impact on the response of the thermosphere and ionosphere to energy and momentum inputs.

We are now working on including the effects of thermospheric winds and the Earth's rotation on the electric potential feedback to the magnetosphere. The next step after that will be the transition to a full description of ionospheric electrodynamics using a new high-resolution version of the NCAR TIE-GCM

(Richmond et al., 1992). Extension of that model to higher altitudes and the addition of a plasmasphere model are also an important aspect of this development. Plasmaspheric density plays an important role in determining the characteristics of ULF waves that have, in turn, significant impacts on the transport and energization of the radiation belt particles. The plasmasphere also interacts with ring current energetic particles through Coulomb collisions that could be important in ring current models such as the rice convection model, which is in the process of being included in the CMIT model (Toffoletto et al., 2004).

It is, however, important to realize here that the coupling between the magnetosphere and ionosphere remains a very complex and challenging problem. We are just beginning to understand this nonlinear, dynamical system. Advancements in outstanding M–I coupling issues, such as ionospheric mass outflow and the mechanism for particle acceleration, will greatly improve the CISM CMIT model and thus our ability to predict space weather.

Acknowledgements

This material is based upon work supported by CISM, which is funded by the STC Program of the National Science Foundation under Agreement Number ATM-0120950. The National Center for Atmospheric Research is sponsored by NSF.

References

Burns, A.G., Killeen, T.L., Roble, R.G., 1991. A theoretical study of thermospheric composition perturbations during an impulse geomagnetic storm. Journal of Geophysical Research 96, 14153–14167.

Burns, A.G., Killeen, T.L., Wang, W., Roble, R.G., 2004. The solar-cycle-dependent response of the thermosphere to geomagnetic storms. Journal of Atmospheric and Solar-Terrestrial Physics 66, 1–14.

Codrescu, M.V., Fuller-Rowell, T.J., Foster, J.C., Holt, J.M., Cariglia, S.J., 2000. Electric field variability associated with the Millstone Hill electric field model. Journal of Geophysical Research 105, 5265–5274.

Daglis, I.A., 1997. The role of magnetosphere-ionosphere coupling in magnetic storm dynamics. In: Tsurutani, B., Gonzalez, W.D., Kamide, Y., Arballo, J.K. (Eds.), Geomagnetic Storms (Geophysical Monograph 98). AGU, Washington, DC, pp. 107–116.

Deng, W., Killeen, T.L., Burns, A.G., Roble, R.G., 1991. The flywheel effect: ionospheric currents after a geomagnetic storm. Geophysical Research Letters 18, 1845–1848.

Dickinson, R.E., Ridley, E.C., Roble, R.G., 1981. A three-dimensional time dependent general circulation model of the thermosphere. Journal of Geophysical Research 86, 1499–1512.

Fedder, J.A., Lyon, J.G., 1987. The solar wind-magnetosphere-ionosphere current-voltage relationship. Geophysical Research Letters 14, 880–883.

Fedder, J.A., Lyon, J.G., 1995. The Earth's magnetosphere is 165 R_E long: self-consistent currents, convection, magnetospheric structure, and process for northward interplanetary magnetic field direction. Journal of Geophysical Research 100, 3623–3636.

Fedder, J.A., Lyon, J.G., Slinker, S.P., Mobarry, C.M., 1995. Topological structure of the magnetotail as a function of interplanetary magnetic field direction. Journal of Geophysical Research 100, 3613–3622.

Foster, J.C., Holt, J.M., Musgrove, R.G., 1986. Ionospheric convection associated with discrete levels of particle precipitation. Geophysical Research Letters 13, 656–659.

Fuller-Rowell, T.J., Codrescu, M.V., Rishbeth, H., Moffett, R.J., Qeugan, S., 1994. Response of the thermosphere and ionosphere to geomagnetic storms. Journal of Geophysical Research 99, 3893–3914.

Hamilton, D.C., Gloeckler, G., Ipavich, F.M., Studemann, W., Wilken, B., Kremser, G., 1988. Ring current development during the great geomagnetic storm of February 1986. Journal of Geophysical Research 93, 14343–14355.

Heelis, R.A., Lowell, J.K., Spiro, R.W., 1982. A model of the high-latitude ionospheric convection pattern. Journal of Geophysical Research 87, 6339–6345.

Killeen, T.L., 1987. Energetics and dynamics of the Earth's thermosphere. Reviews of Geophysics 25, 433–454.

Killeen, T.L., Roble, R.G., 1984. An analysis of the high latitude thermospheric wind pattern calculated by a Thermospheric General Circulation Model 1, Momentum forcing. Journal of Geophysical Research 89, 7509–7522.

Knight, S., 1983. Parallel electric fields. Planetary and Space Sciences 21, 741–750.

Lotko, W., 2004. Inductive magnetosphere-ionosphere coupling. Journal of Atmospheric and Solar-Terrestrial Physics, this issue.

Lu, G., Richmond, A.D., Emery, B.A., Roble, R.G., 1995. Magnetosphere–ionosphere–thermosphere coupling: effect of neutral winds on energy transfer and field-aligned current. Journal of Geophysical Research 100, 19643–19659.

Lyon, J.G., Fedder, J.A., Mobarry, C.M., 2004. The Lyon–-Fedder–Mobarry (LFM) global MHD magnetospheric simulation code. Journal of Atmospheric and Solar-Terrestrial Physics, this issue.

Lyons, L.R., Killeen, T.L., Walterscheid, R.G., 1985. The neutral wind "flywheel" as a source of quiet-time, polar cap currents. Geophysical Research Letters 12, 101–104.

Matsuo, T., Richmond, A.R., Hensel, K., 2003. High-latitude ionospheric electric field variability and electric potential derived from DE-2 plasma drift measurements: dependence on IMF and dipole tilt. Journal of Geophysical Research 108, 1005 doi:10.1029/2002JA009429.

Peymirat, C., Richmond, A.D., Emery, B.A., Roble, R.G., 1998. A magnetosphere-thermosphere-ionosphere electrodynamics general circulation model. Journal of Geophysical Research 103, 17467–17477.

Peymirat, C., Richmond, A.D., Roble, R.G., 2002. Neutral wind influence on the electrodynamic coupling between the

ionosphere and the magnetosphere. Journal of Geophysical Research 107, 1006 doi:10.1029/2001JA900106.

Ponthieu, J.J., Killeen, T.L., Lee, K.M., Carignan, G.R., Hoegy, W.R., Brace, L.H., 1988. Ionosphere–thermosphere coupling at solar maximum and minimum from DE-2 and AE-C data. Physica Scripta 37, 447–454.

Prölss, G.W., 1980. Magnetic storm associated perturbations of the upper atmosphere: recent results obtained from satellite-borne gas analyzers. Reviews of Geophysics 18, 183–201.

Prölss, G.W., 1987. Storm induced changes in the thermospheric composition at middle latitudes. Planetary and Space Sciences 35, 807–811.

Raeder, J., Wang, Y., Fuller-Rowell, T.J., 2001. Geomagnetic storm simulation with a coupled magnetosphere–ionosphere–thermosphere model. In: Song, P., Singer, H., Siscoe, G. (Eds.), Space Weather (Geophysical Monograph 125). American Geophysical Union, Washington, DC, pp. 377–384.

Reiff, P.H., Luhmann, J.G., 1986. Solar wind control of the polar cap potential. In: Kamide, Y., Slavin, J.A. (Eds.), Solar Wind-Magnetosphere Coupling. Terra Sci., Tokyo, p. 453.

Richmond, A.D., Kamide, Y., 1988. Mapping electrodynamic features of the high-latitude ionosphere from localized observations: technique. Journal of Geophysical Research 93, 5741–5759.

Richmond, A.D., Ridley, E.C., Roble, R.G., 1992. A thermosphere/ionosphere general circulation model with coupled electrodynamics. Geophysical Research Letters 19, 601–604.

Ridley, A.J., Richmond, A.D., Gombosi, T.I., DeZeeuw, D.L., Clauer, C.R., 2003. Ionospheric control of the magnetospheric configuration: thermospheric neutral winds. Journal of Geophysical Research 108, 1328 doi:10.1029/2002JA009464.

Robinson, R.M., Vondrak, R.R., Miller, K., Dabbs, T., Hardy, D., 1987. On calculating ionospheric conductances from the flux and energy of precipitating electrons. Journal of Geophysical Research 92, 2565–2569.

Roble, R.G., Ridley, E.C., 1987. An auroral model for the NCAR thermospheric general circulation model (TGCM). Annales Geophysicae 5 (A), 369–382.

Roble, R.G., Ridley, E.C., Richmond, A.D., Dickinson, R.E., 1988. A coupled thermosphere/ionosphere general circulation model. Geophysical Research Letters 15, 1525–2528.

Sojka, J.J., Schunk, R.W., Bowline, M.D., Chen, J., Slinker, S., Fedder, J., 1997. Driving a physical ionospheric model with a magnetospheric MHD model. Journal of Geophysical Research 102, 22,209–22,220.

Spence, H., Baker, D., Burns, A.G., Guild, T., Huang, C.-L., Siscoe, G., Weigel, R., 2004. CISM metrics plan and initial model validation results. Journal of Atmospheric and Solar-Terrestrial Physics, this issue.

Thayer, J.P., Semeter, J., 2004. The convergence of magnetospheric energy flux in the polar atmosphere. Journal of Atmospheric and Solar-Terrestrial Physics, in press.

Thayer, J.P., Vickrey, J.F., Heelis, R.A., Gary, J.B., 1995. Interpretation and modeling of the high-latitude electromagnetic energy flux. Journal of Geophysical Research 100, 19715–19728.

Toffoletto, F.R., Sazykin, S., Spiro, R.W., Wolf, R.A., Lyon, J.G., 2004. RCM meets LFM: initial results of one-way coupling. Journal of Atmospheric and Solar-Terrestrial Physics, this issue.

Wang, W., Killeen, T.L., Burns, A.G., Roble, R.G., 1999. A high resolution, three-dimensional, time dependent, nested grid model of the coupled thermosphere-ionosphere. Journal of Atmospheric and Solar-Terrestrial Physics 61, 385–397.

Wang, W., Killeen, T.L., Burns, A.G., Reinisch, B.W., 2001. A real-time model-observation comparison of F_2 electron densities during the Upper Atmospheric Research Collaboratory campaign of October 1997. Journal of Geophysical Research 106, 21077–21082.

Weimer, D.R., 1995. Models of high-latitude electric potentials derived with a least error fit of spherical harmonic coefficients. Journal of Geophysical Research 100, 19595–19607.

Wiltberger, M., Wang, W., Burns, A.G., Solomon, S., Lyon, J.G., Goodrich, C.C., 2004. Initial results from the coupled magnetosphere ionosphere thermosphere model: Magnetosphere and ionosphere responses. Journal of Atmospheric and Solar-Terrestrial Physics, this issue.